



Intraseasonal variability in the summer South China Sea: Wind jet, cold filament, and recirculations

Shang-Ping Xie,¹ Chueh-Hsin Chang,¹ Qiang Xie,² and Dongxiao Wang²

Received 21 March 2007; revised 2 June 2007; accepted 16 July 2007; published 9 October 2007.

[1] A recent study shows that the blockage of the southwest monsoon by the mountain range on the east coast of Indochina triggers a chain of ocean-atmospheric response, including a wind jet and cold filament in the South China Sea (SCS). We extend this climatological analysis by using higher temporal resolution (weekly) to study intraseasonal variability in summer. Our analysis shows that the development of the wind jet and cold filament is not a smooth seasonal process but consists of several intraseasonal events each year at about 45-day intervals. In a typical intraseasonal event, the wind jet intensifies to above 12 m/s, followed in a week by the development of a cold filament advected by an offshore jet east of South Vietnam on the boundary of a double gyre circulation in the ocean. The double gyre circulation itself also strengthens in response to the intraseasonal wind event via Rossby wave adjustment, reaching the maximum strength in 2 to 3 weeks. The intraseasonal cold filaments appear to influence the surface wind, reducing the local wind speed because of the increased static stability in the near-surface atmosphere. To first order, the above sequence of events may be viewed as the SCS response to atmospheric intraseasonal wind pulses, which are part of the planetary-scale boreal summer intraseasonal oscillation characterized by the northeastward propagation of atmospheric deep convection. The intraseasonal anomalies of sea surface temperature and precipitation are in phase over the SCS, suggesting an oceanic feedback onto the atmosphere. As wind variations are now being routinely monitored by satellite, the lags of 1–3 weeks in oceanic response offer useful predictability that may be exploited.

Citation: Xie, S.-P., C.-H. Chang, Q. Xie, and D. Wang (2007), Intraseasonal variability in the summer South China Sea: Wind jet, cold filament, and recirculations, *J. Geophys. Res.*, *112*, C10008, doi:10.1029/2007JC004238.

1. Introduction

[2] The South China Sea (SCS) is located at the southwest corner of the North Pacific Ocean (99°E–121°E, 0°N–23°N) with an average depth over 2000 m. The SCS is fenced by mountain ranges to its southwest and northeast (Figure 1). On the southwest side, the Annam Cordillera, a coastal mountain range with an average height of 640 m, stretches 1130 km along the borders of Laos and Vietnam and ends just north of Ho Chi Minh City (107°E, 11°N). On the northeast side, the Cordillera Central extends 270 km on northern Luzon Island. The orographic effect of these mountain ranges significantly affects the SCS atmosphere-ocean coupled system [Xie *et al.*, 2003; Wang, 2004; Xie *et al.*, 2006].

[3] The SCS climate is part of the East Asian monsoon system. The prevailing winds are southwesterly in summer

and northeasterly in winter [Liu and Xie, 1999]. The basin-scale upper ocean circulation of the SCS is mainly driven by the seasonal monsoon winds [Wyrki, 1961; Xu *et al.*, 1982; Gan *et al.*, 2006], with significant influence from the Luzon Strait transport [Qu, 2000] and the complex bathymetry including the broad Sunda Shelf (<100 m) in the south [Chu *et al.*, 1999; Cai *et al.*, 2002]. In winter, in response to the strong positive curl of the northeast monsoon, a single cyclonic gyre occupies the basin embedded with two cyclonic eddies: the West Luzon and East Vietnam eddies [Qu, 2000; Liu *et al.*, 2001]. In summer, the Annam Cordillera, impinged by the southwest monsoon, forces a wind jet southeast of Ho Chi Minh City [Xie *et al.*, 2003]. The resultant wind curl dipole drives a double gyre in the ocean, with a northern cyclonic gyre, a southern anticyclonic gyre, and an eastward jet on the intergyre boundary between 11°N and 14°N [Shaw and Chao, 1994; Shaw *et al.*, 1999; Kuo *et al.*, 2000; Ho *et al.*, 2000; Fang *et al.*, 2002; Metzger, 2003]. A tight anticyclonic recirculation, called the South Vietnam eddy, appears at the northwest corner of the southern gyre [Xie *et al.*, 2003; Wang *et al.*, 2006]. The annual mean surface mixed layer depth in the SCS is about 40 m, with little seasonal variability throughout most of the basin [Chao *et al.*, 1996; Qu, 2001].

¹International Pacific Research Center and Department of Meteorology, University of Hawaii, Honolulu, Hawaii, USA.

²Laboratory for Tropical Marine Environmental Dynamics, South China Sea Institute of Oceanology, Chinese Academy of Sciences, Guangzhou, China.

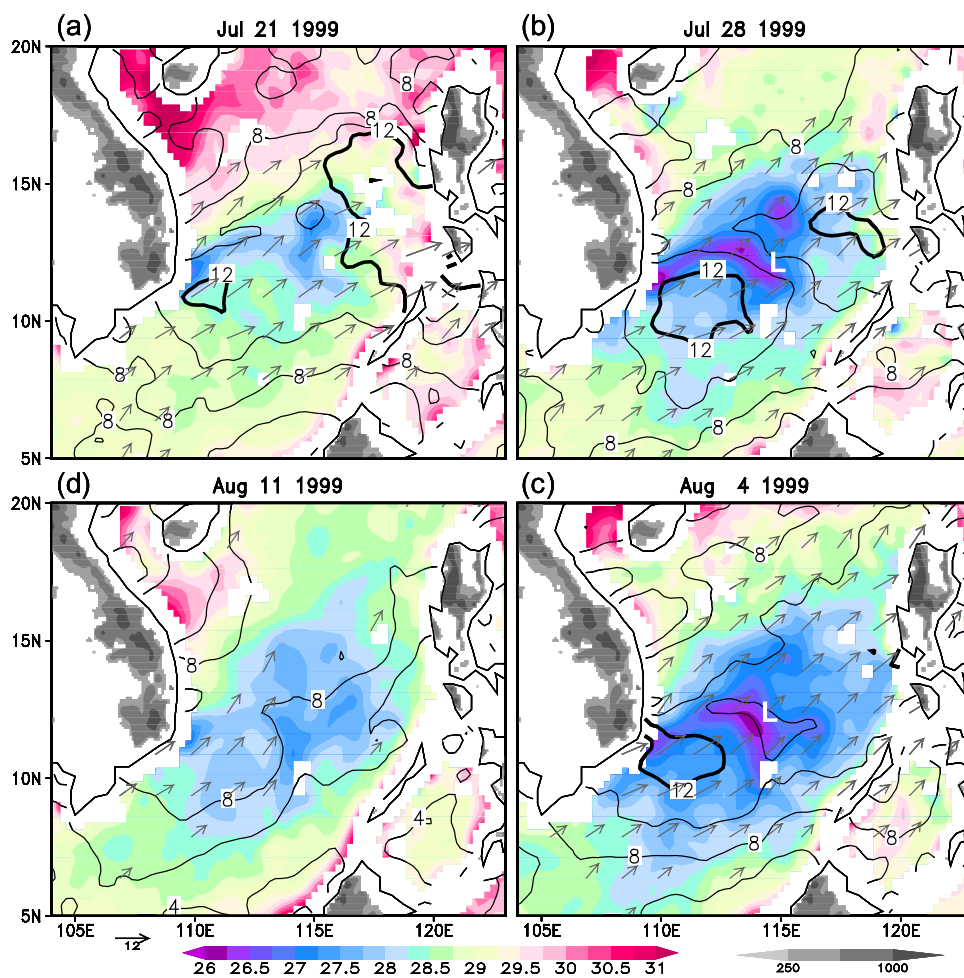


Figure 1. A summer intraseasonal event in 1999 from 21 July to 11 August. The evolution of the cold filament (SST in $^{\circ}\text{C}$, color shading), and surface wind speed (ms^{-1} , contour). The gray shading indicates the land orography greater than 250 m. The vector indicates surface wind greater than 4 m/s. Local wind speed minimum over the cold filament is marked with a white “L.”

[4] The SCS warms up rapidly in spring as part of the planetary-scale Indo-western Pacific warm pool [Wang and Wang, 2006]. In summer, a pronounced basin-scale cooling is observed in the SCS and was traditionally attributed to evaporative cooling by the southwest monsoon [Qu, 2000]. High-resolution satellite observations of sea surface temperature (SST) reveal coastal upwelling along South Vietnam and a cold filament that stretches eastward at about 12°N from the coast superimposed on the basin-scale cooling [Kuo *et al.*, 2000; Ho *et al.*, 2000]. The orographic-induced southwest wind jet is key to the cold filament’s offshore development, by inducing coastal upwelling and driving the eastward ocean jet that advects the cold coastal water offshore [Xie *et al.*, 2003].

[5] In a climatological analysis of multiyear satellite observations, the cold filament begins to develop in June, strengthens and reaches the maximum intensity in July–August, and disappears in September [Xie *et al.*, 2003]. The Asian summer monsoon, on the other hand, is known to display large intraseasonal oscillations [Wang, 2006; Lau and Waliser, 2005]. Strong intraseasonal variability in wind and SST has been reported in the Bay of Bengal [Sengupta *et al.*, 2001; Vecchi and Harrison, 2002], the West Arabian

Sea [Vecchi *et al.*, 2004], and the SCS [Gao and Zhou, 2002]. The Gao and Zhou study uses coarse-resolution data that do not resolve important features such as the cold filament and ocean advective effects in general.

[6] The present study examines intraseasonal variability in the summer SCS using a suite of new satellite datasets of high resolution in space and time. We show that the cold filament does not simply persist through the summer but instead experiences 2–3 cycles of development and decay. This intraseasonal variability in SST may simply be a response to intraseasonal wind variability or alternatively due to internal variability of the double gyre circulation. In models, nonlinear interaction of the western boundary currents, recirculations and potential vorticity advection is known to cause chaotic variability of the intergyre eastward jet (see Dijkstra and Ghil [2005] for a review), which may then cause the cold filament to fluctuate. To investigate these possibilities, our study will examine variability in wind and sea surface height (SSH) as well as their relationship to the intraseasonal development of the cold filament. Our analysis supports the wind-forced hypothesis.

[7] The organization of the paper is as follows. Section 2 describes the data sets. Section 3 investigates oceanic

variability by a case study, variance, and composite analyses. Section 4 explores the origin of intraseasonal wind variability over the SCS using a lag regression analysis. Section 5 examines the feedback of cold filaments on the atmospheric boundary layer. Section 6 summarizes the findings and discusses their implications.

2. Data

[8] We use weekly mean data to suppress synoptic disturbances. The primary data sets include SST from a satellite microwave radiometer, surface wind from a satellite scatterometer, and SSH anomalies from satellite altimeters.

[9] Launched in November 1997, the Tropical Rainfall Measuring Mission (TRMM) Microwave Imager (TMI) is a passive microwave sensor with a suite of channels ranging from 10.7 to 85 GHz that measures microwave energy emitted by the Earth and its atmosphere to quantify important atmospheric variables, such as water vapor, cloud water, and rainfall intensity. The addition of a low-frequency channel at 10.7 GHz (almost cloud transparent) enables the TMI to measure the SST in all weather conditions except under heavy rain. The TMI provides complete coverage of the global tropics (38°S–38°N) every three days. The accuracy of the TMI SST estimate in rain-free conditions is approximately 0.6°C [Wentz *et al.*, 2000]. In this study, the weekly $0.25^\circ \times 0.25^\circ$ gridded TMI SST data (version 3a) are used from 10 December 1997 to 29 December 2004.

[10] A scatterometer measures the backscatter from short water waves (i.e., capillary and ultragravity waves), which respond quickly to changes in winds, to derive near-surface wind speeds and directions. Since July 1999, the SeaWinds scatterometer on the QuikSCAT satellite has been providing global wind measurements with high spatial and temporal resolution under almost all weather conditions except for heavy rain. The SeaWinds scatterometer wind retrievals are accurate to better than 2 m/s in speed and 20° in direction, accuracies comparable to in-situ point measurements from buoys [Chelton *et al.*, 2004]. We use the weekly averaged QuikSCAT data on a $0.25^\circ \times 0.25^\circ$ grid from 21 July 1999 to 29 December 2004.

[11] Satellite altimetric measurements of sea surface topography contain large geoid undulations, which are not well determined. One can deduce deviations from the absolute SSH and study temporal variations of the ocean circulation. We use the weekly averaged merged SSH anomalies (SSHA) from the TOPEX/Poseidon (T/P), Jason, ERS-1, ERS-2, and ENVISAT satellites on a $0.33^\circ \text{lon} \times 0.18^\circ \text{lat}$ grid from 14 October 1992 to 29 December 2004. The merged SSHA better resolves spatial and temporal scales of the ocean circulation, especially the mesoscale, than using one single altimeter [Ducet *et al.*, 2000]. Launched on 10 August 1992, the T/P altimeter achieved an unprecedented accuracy of about 4 cm. Much smaller SSH signals (~ 1 cm) of large spatial scales may be detected with random measurement errors filtered out. We obtain the absolute SSH by adding a recent 10-year mean SSH field to the merged T/P SSHA data. The time-mean SSH is computed using near-surface velocity derived from surface drifter data and satellite altimeter observations [Niiler *et al.*, 2003].

[12] To map planetary-scale atmospheric patterns, two additional data sets are used: the European Center for Medium-Range Weather Forecasting reanalysis (ERA) of daily geopotential height and wind at 850 hPa for the period of 14 October 1992 to 28 August 2002, and the pentad-mean Climate Prediction Center merged analysis of precipitation (CMAP) [Xie and Arkin, 1997] for the period 14 October 1992 to 20 December 2004. Both data sets are on a $2.5^\circ \times 2.5^\circ$ grid. To be compatible with the primary satellite data sets, the daily ERA and pentad CMAP data are processed into weekly mean values.

[13] In the composite and regression analyses, we remove the seasonal cycle by subtracting the monthly climatology from the weekly mean data (after a temporal interpolation). A 90-day high-pass filter is then applied to isolate intraseasonal variability. Such filters are commonly used in intraseasonal variability studies and appropriate for variability over the SCS, which as will be seen, has typical timescales of 6–7 weeks.

3. Oceanic Variability

[14] We begin with a case study to introduce the intraseasonal phenomenon, followed by variance and composite analyses to extract its spatiotemporal characteristics.

3.1. Case Study

[15] Figure 1 shows the intraseasonal evolution of the SST and the wind fields from the week of 21 July 1999 to that of 11 August 1999. It is the first intraseasonal event after the QuikSCAT began its science operation. In the third week of July 1999, the orographically induced wind jet (>12 m/s) appears off of Ho Chi Minh City centered at 111°E , 11°N , with large positive wind curls to the north. Cold water ($<27.5^\circ\text{C}$) pumped up via the coastal upwelling mechanism is seen in the coastal region between 11.5°N and 12.5°N , north of the wind jet. A long thin arc of cold water ($<28^\circ\text{C}$), the cold filament, stretches offshore from the coast and curves to the southeast as it reaches the open ocean (Figure 1a). The wind jet intensifies in the following week and remains strong until the week of 4 August. The arcing cold filament continues to strengthen, reaching the maximum intensity with a minimum SST of 26.5°C 1 week after the wind jet begins to wane. By the week of 11 August (2 weeks after the maximum wind speed), the wind relaxes (≤ 8 m/s), and the cold filament diffuses, leaving behind a broad pool of relatively cold water (SST $< 28^\circ\text{C}$) over much of the central SCS (Figure 1d).

[16] Figure 2 superimposes SST (color) on the SSH field (in contour) during the week of 28 July 1999. A pair of recirculation eddies are present, with their boundary around 12°N . The cold filament is anchored on the South Vietnam coast and advected offshore, riding on the northern rim of the anticyclonic southern recirculation eddy. The distinct arc structure of the cold filament and its curving to the south suggest that the water originating from the western boundary of the southern gyre does not mix readily with water from the northern gyre presumably because of their distinct potential vorticity [Wang *et al.*, 2002]. The southern gyre western boundary current and its extension advect water of low potential vorticity from the south while the northern gyre western boundary current advects high potential

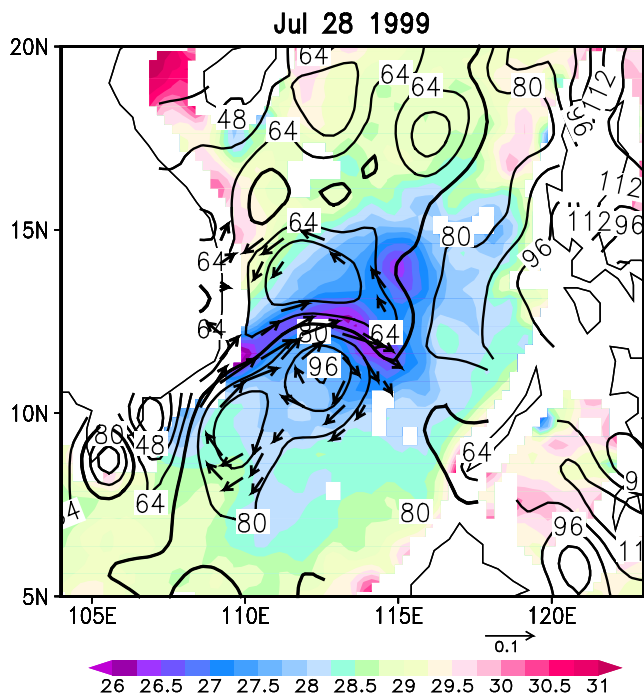


Figure 2. Same intraseasonal event as in Figure 1: SST ($^{\circ}\text{C}$ color shading) superimposed on SSH (cm, contour) on 28 July 1999. The vector indicates the geostrophic currents associated with the double gyre system (7° – 15°N , 108° – 115°E). The 72 cm contour is in bold, which conveniently marks the gyre boundary.

vorticity. The potential vorticity gradients on the gyre boundary discourage cross-gyre mixing.

3.2. Variance Analysis

[17] Figure 3 shows time-latitude sections of wind speed (contours) and SST (color) along 111°E , a longitude cutting across cold filaments. From 1999 to 2004, every summer from May to September, there are two to four cooling

events. Each one is associated with a strong basin-wide wind pulse ($>8\text{ m/s}$) and a temperature drop of at least 1°C – 1.5°C . ISV in non-El Nino years of 2000–2002 is similar to that in 1999 and 2004 (not shown). Note that compared to those in other years, summer intraseasonal events are weak in 2003 because the seasonal mean southwest monsoon weakens following the 2002 El Nino [Xie et al., 2003]. In the summer following the major El Nino event of 1997–1998, the SCS is abnormally warm, and no intraseasonal development of the cold filament is observed.

[18] We have calculated the root mean square (RMS) variance of surface wind speed, SST, and SSH by using the 90-day high-pass filtered data for their respective available periods. The variance is accumulated during June to August (JJA) for SST and wind, and June–September (JJAS) for SSH. The double gyre circulation persists through the summer after the southwest monsoon begins to weaken in August. Figure 4 shows the results (color) superimposed on their long-term summer means (contours).

[19] The maximum summer mean wind (speed $>9\text{ m/s}$) is located southeast of Ho Chi Mihn City with its core at (110°E , 10.5°N), a result of orographic blockage by the Annam mountain range [Xie et al., 2003]. The RMS variance of wind, however, displays a pattern different from the mean jet, with large values ($>2.3\text{ m/s}$) displaced further east in the open ocean in 112°E – 118°E , 9.5°N – 12°N (Figure 4a). Orographic effects on intraseasonal winds are still visible; the wind variance nearly vanishes lee of the Annam range, generating larger wind curls north than south of 11°N . Section 4 discusses how large-scale atmospheric patterns give rise to intraseasonal wind fluctuations over the SCS.

[20] In the summer mean, the double gyre circulation forms in the ocean in response to the wind curl forcing of the southwest wind jet [e.g., Wang et al., 2006]. The maximum SSH variability ($>5.6\text{ cm}$) is located between 11°N and 12°N , slightly north of the gyre boundary (11°N ; Figure 4b). This variance maximum may reflect internal variability of the nonlinear double gyre circulation that tends to peak at the gyre boundary [e.g., Taguchi et al.,

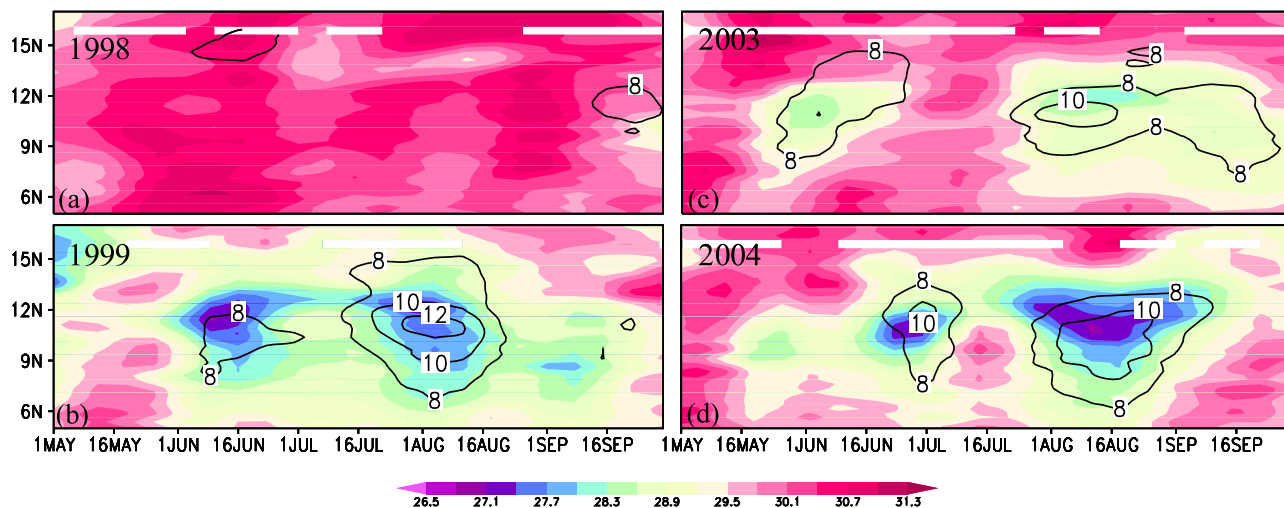


Figure 3. Summer intraseasonal pulses seen in time-latitude sections of SST ($^{\circ}\text{C}$, color shading) and wind speed (ms^{-1} , contour) at 111°E for the summer (May to September) of (a) 1998, (b) 1999, (c) 2003, and (d) 2004.

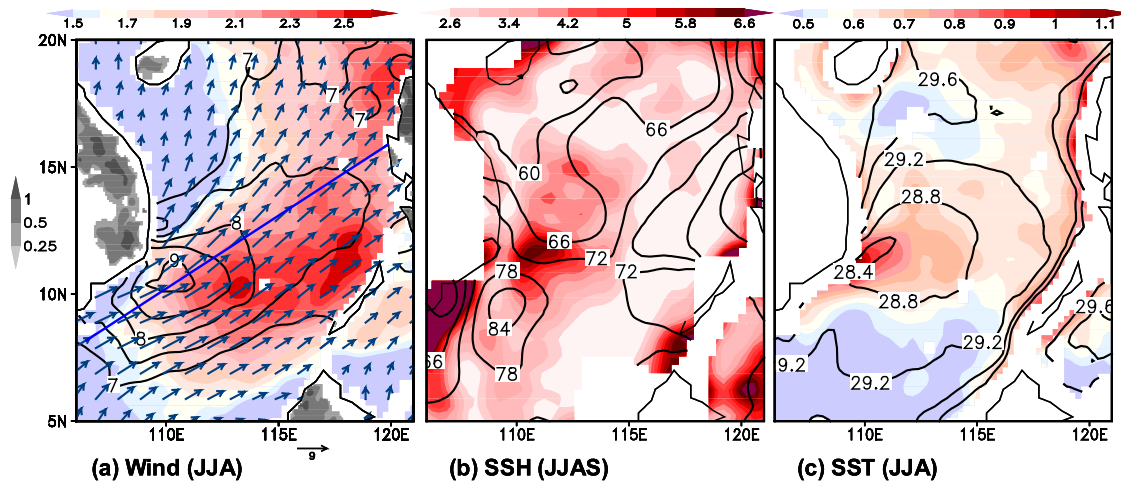


Figure 4. Standard deviation of intraseasonal anomaly (90-day highpass filtered data; shading) versus climatological mean (contour) in summer (JJA) for 1999–2004: (a) surface wind speed (ms^{-1}); (b) SSH (cm); and (c) SST ($^{\circ}\text{C}$). In Figure 4a the gray shading indicates the land orography greater than 0.25 km, and the vectors are for climatological wind velocity.

2007], or it may simply be a response to the asymmetric wind-curl forcing that is stronger north of 11°N due to the orographic blockage as discussed above. In subsection 3.3.2, we will trace the intraseasonal evolution of SSH anomalies to examine these two possibilities.

[21] The maximum upwelling cooling is located near 11°N on the South Vietnam coast. The region of large intraseasonal SST variability ($\text{RMS} > 0.8^{\circ}\text{C}$) is collocated with the mean cold filament, both displaying a distinctive northeastward development from the Vietnam coast (Figure 4c). Further offshore, the curving arc is not present in the mean SST map, indicating its variability in position.

3.3. Composite Evolution

[22] This subsection tracks the evolution of SCS intraseasonal variability (ISV) in the ocean and atmosphere by constructing lagged composite maps based on an ISV index defined as wind speed anomalies averaged in the box of 112°E – 116°E , 9°N – 13°N , where wind ISV is high. The use of an alternative SST index averaged in its high variance region off the Vietnam coast yields similar results. For the composite analysis, 10 strong intraseasonal wind events with 90-day high-pass filtered speed anomalies greater than

0.6 standard deviation are chosen for the period of June to August 1999–2004.

3.3.1. SST and Wind

[23] Figure 5 shows the composite anomalies of wind speed (contours) and SST (color). At lag -1 week, winds are calm and SST above the climatology. In the following week, the southwest winds intensify rapidly by 2 m/s over much of the SCS, with the maximum increase of 3.5 m/s in the open-ocean just west of Palawan Island. SST begins a basin-wide cooling of $\sim 0.3^{\circ}\text{C}$ in response to this intraseasonal wind pulse. At lag $+1$ week, this wind pulse weakens considerably while the SST cooling reaches its maximum, with a distinct offshore development of the cold filament from the Vietnam coast. SST anomalies in the cold filament are about -1°C in the filament. The arc structure of the cold filament, however, is unclear in the composite because of position variations from one event to another. At lag $+2$, winds relax further, and SST returns to near normal. Overall, an intraseasonal wind event lasts for 2 weeks, and the cold filament development lags by 1 week.

3.3.2. SSH

[24] Figure 6 shows the evolution of composite SSH anomalies when and after the southwest monsoon intensi-

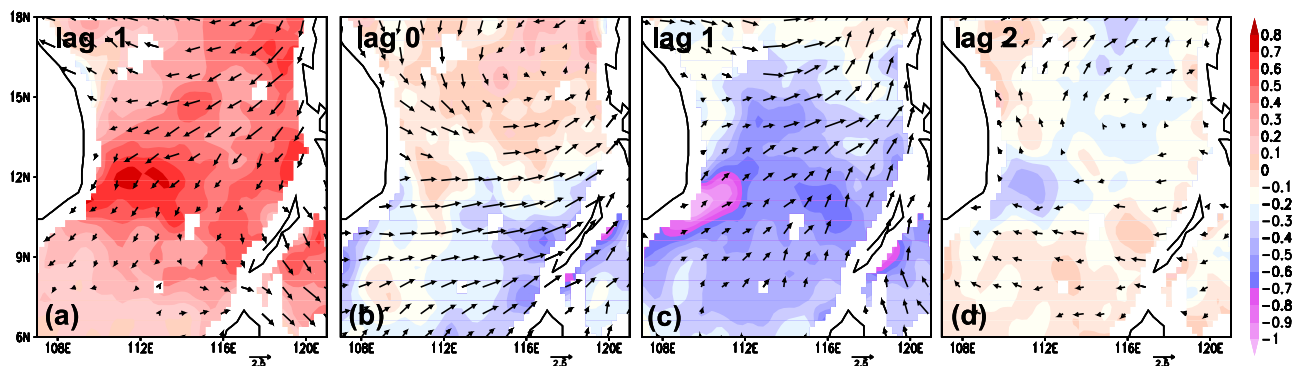


Figure 5. Summer intraseasonal event composites of SST ($^{\circ}\text{C}$, color shading) and wind speed (ms^{-1} ; solid (positive) and broken (negative) contours), based on 10 strong wind events (summer ISV wind index ≥ 0.6 std) during six summers (JJA) from 1999 to 2004. Time lags are in week.

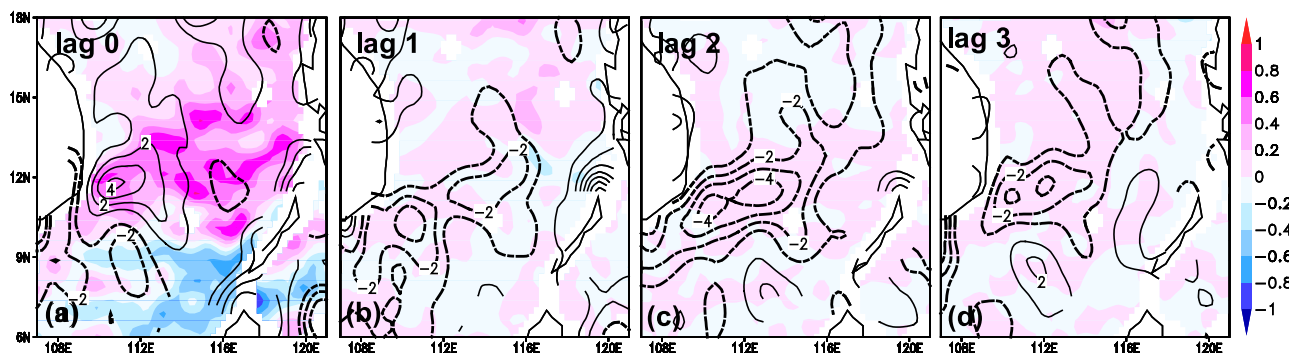


Figure 6. Same as in Figure 5 but for wind stress curl (10^{-7} Nm^{-3} , color shading) and SSH (cm, +SSHA in solid, and -SSHA in broken contours) for (a) lag 0, (b) lag 1, (c) lag 2, and (d) lag 3.

fies. At lag 0, there is a pair of anomalous circulations off the Vietnam coast, likely remnants of the previous intraseasonal cycle at the phase of weakened southwest monsoon. They are anticyclonic north and cyclonic south of 10.5°N , representing a weakening of the seasonal mean double gyre circulation. At lag +1 week, the southern negative SSH anomalies somewhat strengthen while the northern anomalous circulation disappears near the coast. Negative SSH anomalies develop to the east around 114°E , 11.5°N , likely in response to the strong positive wind curls at lag 0. At lag 2, these newly formed negative SSH anomalies strengthen to -4 cm and move westward near the Vietnam coast. At lag 3, these negative SSH anomalies weaken slightly and are confined in the western half of the SCS north of 10°N , representing an intensification and southward shift of the offshore jet. To the south, weak positive anomalies of 2 cm begin to appear around 112°E , 8.5°N , which can be traced 2° eastward 1 week earlier.

[25] The above analysis suggests a Rossby wave adjustment of the SCS to changes in wind forcing. Figure 7 illustrates this adjustment with longitude-time sections of anomalies of wind curl and SSH along 12°N . In response to positive wind curl forcing at lag 0, negative SSH anomalies begin to appear in the eastern basin, then strengthen, and propagate westward. It takes 2–3 weeks for the negative SSH anomalies to arrive at the Vietnam coast. From Figure 7, the Rossby wave speed is estimated at 3.7 cm/s at 12°N , equivalent to a 5-week transit time across the basin. This is in rough agreement with modeling studies of Liu *et al.* [2001] and Wang *et al.* [2003, 2006]. It is notable that the amplitude of the wind stress curl in Figures 6 and 7 is large at lag 0 but then this decreases rapidly, although the SSH does not. This is because the wind field is more noisy at the weekly timescale, whereas the ocean response occurs at a lower frequency, so there is less damping of the signal at lag in SSH.

[26] The southwest monsoon is strongest at lag 0. This wind intensification displays a clear blockage effect by the Annam mountains, with wind anomalies decreasing rapidly in the lee (Figure 4b). Wind curls are much stronger north than south of the wind maximum ($0.6 \sim 0.7 \text{ N/m}^3$ versus $-0.2 \sim -0.3 \text{ N/m}^3$), an asymmetry that induces a meridionally asymmetric response in ocean circulation. Indeed, the SSH anomalies north of 11°N are larger and better organized in space (Figure 6).

[27] At both lags 0 and 1, SSH anomalies are such that the double gyre circulation is weaker than normal (Figure 6), ruling out the possibility that the cold filament's eastward development is due to the anomalous increase in the offshore jet and its advection. Instead, the intensification of the double gyre circulation lags that of the southwest monsoon by two weeks, in accordance with the Rossby wave adjustment, after the cold filament has begun decaying. Thus the intraseasonal development of the cold filament is due to the increased coastal upwelling and offshore advection by the mean eastward jet.

4. Origin of SCS ISV

[28] In this section, we look beyond the SCS and identify large-scale atmospheric patterns associated with the intra-

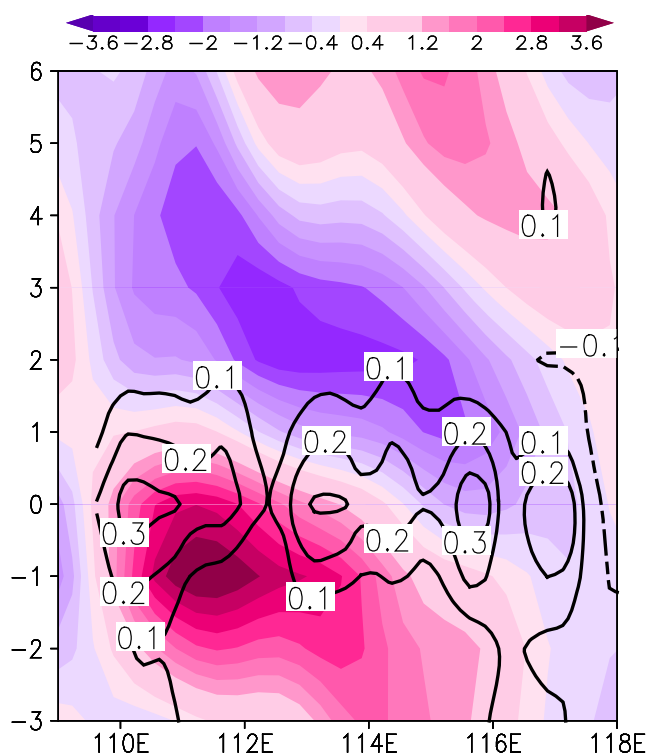


Figure 7. Time-longitude section of SSH (cm, in color shading) and wind stress curl (10^{-7} Nm^{-3} , contour) anomalies along 12°N . Time lags are in week.

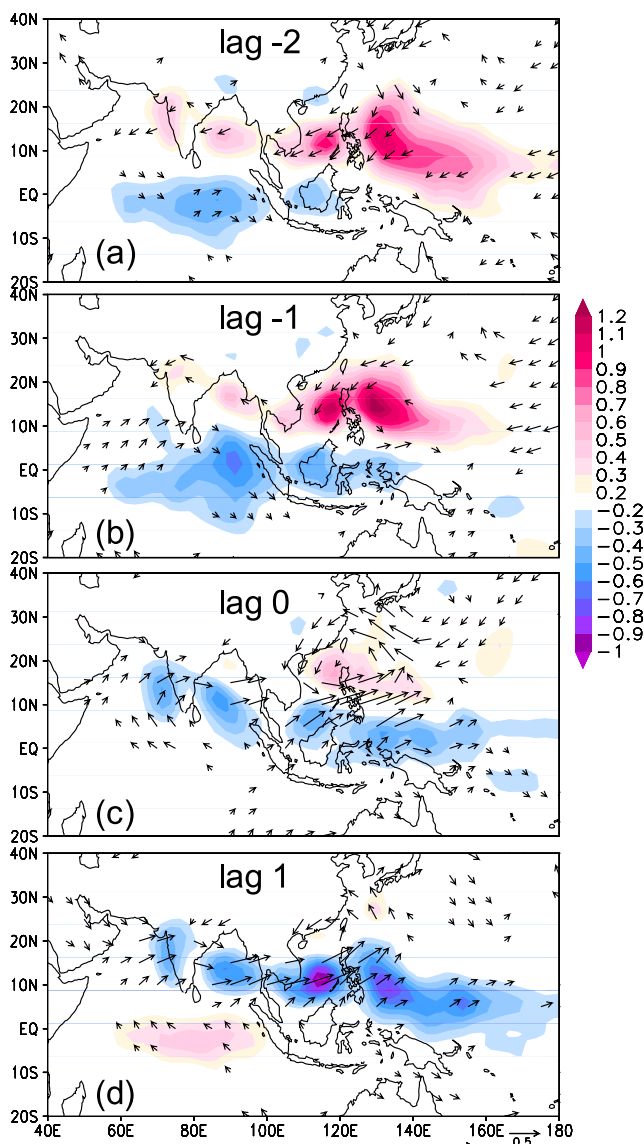


Figure 8. Lag-regression of rainfall (mm/day, color shading) and 850 hPa wind (>0.05 m/s; in vector) upon the ERA wind index during 10 summers (JJA) from 1993 to 2002. Time lags are in week.

seasonal wind variability in the summer SCS. To increase the data length, we use ERA geopotential height and wind velocity (1992–2002) at 850 hPa, a pressure level above most of mountains in the region except the Tibetan Plateau. The SCS ISV indices based on the ERA and QuikSCAT wind products correlate well with each other at 0.84 for their overlapping period. The ERA 850 hPa wind velocity, geopotential height, and the CMAP rainfall are regressed on the SCS summer ISV index based on ERA wind at lag intervals of 1 week.

[29] Figure 8 shows the regression maps of ERA wind (arrows) superimposed on CMAP rainfall (color). At lags -2 and -1 , anomalous winds are northeasterly against the prevailing southwesterlies. A band of positive rainfall anomalies extends in a slight southeast tilt from India and the Bay of Bengal, en route from the SCS to the western

equatorial Pacific. From lag -2 to 0, this rain band moves northward and a center of positive rainfall anomalies forms over the northern SCS and the northwestern tropical Pacific to the east. This center of positive rainfall anomalies, together with negative rainfall anomalies over the equatorial Indian Ocean and the Maritime Continent, drives a strong intensification of the southwesterlies over the central SCS at lag 0 (Figure 8c), in geostrophic balance with large meridional gradients of geopotential height (not shown). Thus anomalies of both wind and geopotential lag behind these rainfall anomalies by 1 week, peaking at lag 0. A strong cyclonic circulation forms centered on the Luzon Strait at lag 0 and persists into lag +1 with reduced intensity. At lag 0, positive rainfall anomalies dissipate, replaced by a tilted band of negative anomalies to the south. Negative rainfall anomalies first appear in the equatorial Indian Ocean at lag -2 , then expand and propagate both eastward along the equator and northward in the Indian Ocean to the SCS sector.

[30] Figure 9 shows Hovmöller diagrams of regressed rainfall anomalies to further illustrate these propagation characteristics of convection. In the longitude-time section along the equator, the eastward propagation is seen from 60°E to 160°E , with some disruption over the Maritime Continent. In the latitude-time section averaged from the Bay of Bengal (80°E) to the SCS (120°E), convective anomalies first appear on the equator and then propagate northward onto the Asian Continent. The average eastward and northward propagation speeds are $4^{\circ}/\text{day}$ and $0.7^{\circ}/\text{day}$, respectively. The former (~ 5 m/s) is typical of atmospheric ISV phase speed. The typical period of the convective oscillation is 6–7 weeks (~ 45 days).

[31] The tilted, zonally elongated anomalous rain band, the eastward propagation along the equator, and the northward propagation in the Bay of Bengal to the SCS sector are all known characteristics of the so-called boreal summer intraseasonal oscillation over South Asia and Indo-western Pacific warm pool region [e.g., *Annamalai and Slingo*, 2001; *Waliser et al.*, 2004; *Jiang et al.*, 2004] (see *Lau and Waliser* [2005] and *Wang* [2006] for recent reviews). In fact, convective ISV displays a local variance maximum in the SCS, and *Straub and Kiladis* [2003] use the time series in this region of maximum as the index for their analysis of planetary-scale ISV. Thus intraseasonal wind variability over the summer SCS is not a local phenomenon but part of planetary-scale organization of atmospheric convection and circulation.

5. Ocean-to-Atmospheric Feedback

[32] To first order, the intraseasonal cooling of the SCS may be considered as the oceanic response to planetary-scale atmospheric ISV but the cold filaments exert a visible effect onto surface wind. For this, we return to the intraseasonal event that lasts for four weeks from late July to early August 1999. During 28 July to 4 August, strong winds above 10 m/s are observed along the wind jet axis that tilts in the northeast direction (Figure 1). The fully developed cold filament disrupts the high wind speed along this axis; during the week of 28 July, wind speed drops by 2–3 m/s to below 10 m/s over the cold filament compared to the values above 12 m/s both up and down wind. This

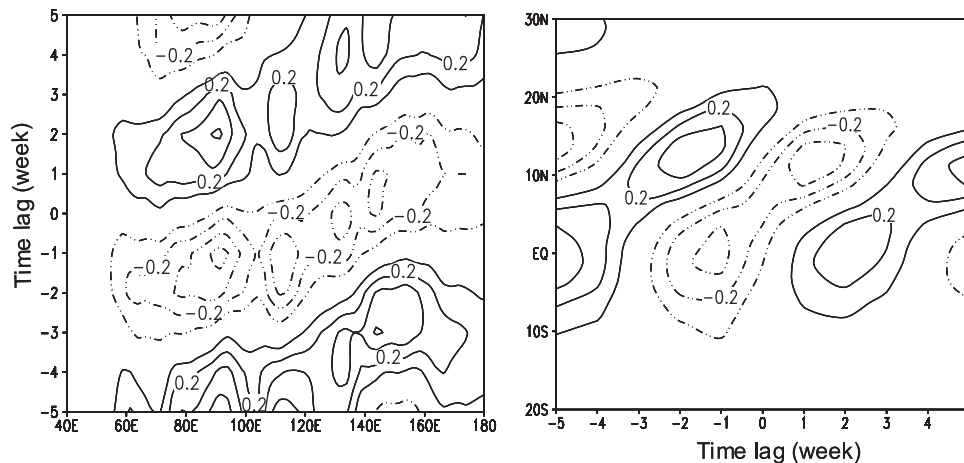


Figure 9. Lag-regression of rainfall anomaly (mm day^{-1}) upon the ISV wind index from week -5 to $+5$: (a) equatorial (5°S – 5°N) time-longitude diagram, and (b) latitude-time diagram in the Bay of Bengal to South China Sea sector (80°E – 120°E).

wind speed minimum persists in the following week over the cold filament, weakening but still visible for another week.

[33] The collocation and coevolution of the cold filament and wind speed minimum are commonly observed in the summer SCS as illustrated by the distance-time sections along the northeast tilted wind jet axis (Figure 10). This axis, taken based on the climatological wind distribution (Figure 4a), intercepts the southward curving part of the filament arc. As another example, a wind speed reduction of 3 m/s is also observed over the cold filament event during late August to early September 2000 (Figure 10b).

[34] The wind response is a negative feedback for the cold filament development: the local wind speed reduction and increased atmospheric stability act to suppress the latent heat flux from the ocean, damping the SST minimum. Such a local wind response to SST variability is commonly observed near major ocean fronts in the world ocean [Xie, 2004; Chelton *et al.*, 2004], including the western Arabian Sea off Somali [Vecchi *et al.*, 2004], the East China Sea [Xie *et al.*, 2002], and the Kuroshio Extension [Nonaka and Xie, 2003]. Lin *et al.* [2003] observe such a wind speed reduction over the summer SCS over the cold wake left behind by a typhoon. Such ocean-to-atmospheric feedback is characterized by a positive correlation between SST and wind speed anomalies and considered to be due to the SST modulation of near-surface atmospheric variability [Xie, 2004]. Over the cold filament, the increased atmospheric stability reduces the surface wind stress and hampers the vertical mixing that would bring faster winds from aloft. Recently, however, Small *et al.* [2005] suggest that the SST-induced pressure anomalies in the boundary layer explain the positive correlation between SST and wind speed if the down-wind advection is considered.

[35] Xie *et al.* [2003] draw an analogy between the western Arabian Sea and SCS during summer in their sharing common features such as an orographic-induced southwest wind jet, a quasi-stationary anticyclonic eddy south of the wind jet, strong coastal upwelling, the offshore development of cold filaments. This analogy becomes even

closer in the local wind response to the cold filament development in both regions [Vecchi *et al.*, 2004].

6. Summary

[36] We have studied intraseasonal variability in the summer SCS using a suite of newly available, cloud-penetrating microwave observations from satellite. The high spatial resolution of these satellite data enables us to study mesoscale features such as the cold filaments and recirculation eddies in the ocean, and the narrow wind jet in the atmosphere. Our analysis shows that the SCS cold filament does not develop smoothly on the seasonal timescale as depicted in the climatological analysis of Xie *et al.* [2003], but instead it experiences pronounced intraseasonal cycles of development and decay during a typical summer in response to the fluctuations of the southwest wind jet. The typical period of such cycles is 6–7 weeks, comparable with the timescales of atmospheric ISV in the region [e.g., Straub and Kiladis, 2003; Jiang *et al.*, 2004]. The intraseasonal cold filament development is subdued or suppressed completely in the summer following an El Niño event as the southwest monsoon weakens.

[37] Our results suggest the following conceptual model for summer ISV over the SCS. Intraseasonal wind variability in the summer SCS is part of a planetary-scale mode of ISV over South Asia and the Indo-Pacific warm pool, characterized by a tilted band of anomalous rainfall that propagates eastward along the equator and northward in the Bay of Bengal to the SCS sector. Following the intensification of atmospheric convection over the central SCS as part of this planetary-scale oscillation, the southwesterlies over the SCS strengthen, causing strong coastal upwelling off South Vietnam in the subsequent week. This cold upwelled water is then advected offshore, forming an arc-shaped filament in SST. The offshore advection is provided by an eastward ocean jet on the boundary of a double gyre circulation forced by the wind curls of the southwest wind jet. The offshore cold filament leaves a visible imprint on the atmosphere, reducing the local wind speed by 2–3 m/s at the sea surface.

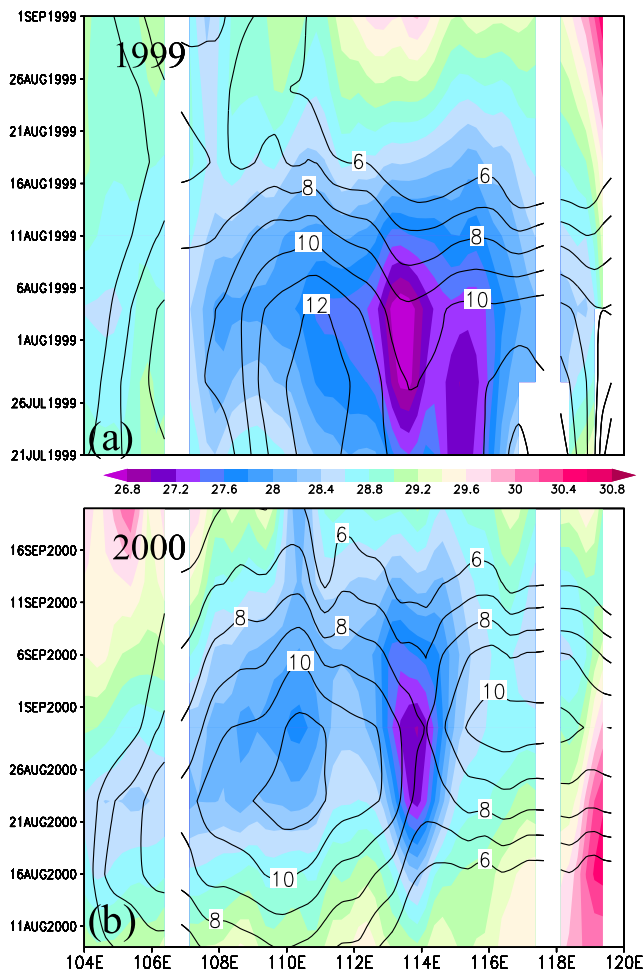


Figure 10. Time-distance diagrams of wind speed (ms^{-1} , contour) and SST ($^{\circ}\text{C}$, color shading) along the mean southwest wind axis as marked in Figure 4a, during two intraseasonal wind events in (a) 1999 and (b) 2000.

[38] Large SSH anomalies of 3–4 cm are observed over the SCS. The strengthening of the double gyre circulation lags behind the wind intensification by 2–3 weeks, a delay due to the westward propagation of ocean Rossby waves. The SSH variability is greater in the northern than the southern gyre because of the asymmetry in wind forcing; the blockage of the southwesterlies by the Annam mountain range is strong in the lee, creating larger wind curls and a stronger SSH response north than south of the axis of the southerly wind acceleration. Thus our composite analysis keyed on a wind index reveals a SCS circulation adjustment consistent with the wind-forced Rossby wave mechanism. By construction, our method finds no evidence for internal variability of the double gyre circulation playing a role in the intraseasonal cold filament development. Instead, the wind-induced variability in the coastal upwelling is the main cause of the intraseasonal development and retreat of the cold filament. In a related study of another intergyre inertial jet, *Taguchi et al.* [2007] reach a similar conclusion that the majority of decadal variability in the Kuroshio Extension jet east of Japan is due to wind-forced baroclinic

Rossby waves despite considerable internal variability. They suggest that low-frequency wind forcing may regulate the inertial jet's internal variability.

[39] Does the intraseasonal cooling of the SCS have any influence on large-scale atmospheric convection and circulation? Our results tentatively suggest a positive answer. In our composite analysis, the SST cooling (Figure 5c) and suppressed atmospheric convection (Figure 8d) both occur at lag 1 week, suggesting that the former possibly forces the latter. Figure 11 confirms that SST leads precipitation by one week over the central SCS on intraseasonal timescales. Similar covariations of SST and convection on intraseasonal timescales have been noted by *Sengupta et al.* [2001] and *Vecchi and Harrison* [2002] over the Bay of Bengal. Furthermore, coupled model experiments of *Fu et al.* [2003] show that the northward propagating ISV weakens in the atmosphere if the interaction with the ocean is suppressed. *Fu et al.* [2003] suggest that the wind-evaporation-SST (WES) feedback is the major mechanism for ocean-atmosphere interaction over the Bay of Bengal on intraseasonal timescales. In fact, the WES mode of air-sea interaction under the prevailing westerly winds displays a poleward phase propagation [*Xie*, 1999], consistent with observations and *Fu et al.*'s model experiments. In the summer SCS, besides surface evaporation, the coastal upwelling and its offshore advection are important mechanisms for SST variability, possibly strengthening ocean-atmosphere interaction there compared to the Bay of Bengal.

[40] Intraseasonal variability is likely not to be limited to physical fields. As the offshore advection carries from the

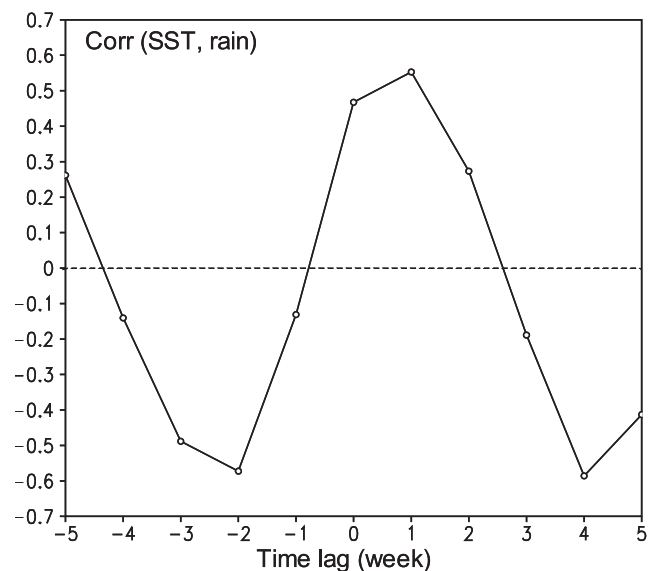


Figure 11. Lag correlation (from lag -5 to $+5$ week) of CMAP precipitation with the reference time series of TRMM SST for JJA 1998–2004, both averaged over 112.5 – 117.5°E , 10 – 15°N . Precipitation leads SST at negative lags. With a typical ISV period of 45 days, we estimate the degree of freedom for the seven-summer time series to be 28, for which the correlation is 95% significant at 0.38 based on student-t test.

Vietnam coast not only the cold upwelled water but also high nutrients [Xie *et al.*, 2003; Tang *et al.*, 2004], it is conceivable that intraseasonal variability in coastal upwelling (the source region for the cold filament) causes fluctuations in offshore nutrients and biological activity over the cold filament. Recently it came to our attention that Isoguchi and Kawamura [2006] has detected such intraseasonal variability in chlorophyll from satellite. As wind variations are now being routinely monitored by satellite, the lags of 1–3 weeks in oceanic response offer useful predictability that may be exploited.

[41] **Acknowledgments.** We wish to thank B. Taguchi for technical assistance, J. Hafner for maintaining a local satellite data archive, and P. Hacker for encouragement and support. The TMI and QuikSCAT data are obtained from the Web site of Remote Sensing Systems. This work was presented at the South China Sea International Workshop in Guilin, China, July 2005 and the AGU Ocean Sciences Meeting, Honolulu, February 2006. This work is supported by NASA, NOAA, the Japan Agency for Marine-Earth Science and Technology, the Chinese Academy of Sciences, and NSFC (40476013 and 40506008). IPRC publication 470 and SOEST publication 7166.

References

- Annamalai, H., and J. M. Slingo (2001), Active/break cycles: diagnosis of the intraseasonal variability of the Asian Summer Monsoon, *Clim. Dyn.*, *18*, 85–102.
- Cai, S. Q., J. L. Su, Z. J. Gan, and Q. Y. Liu (2002), The numerical study of the South China Sea upper circulation characteristics and its dynamic mechanism, in winter, *Cont. Shelf Res.*, *22*, 2247–2264.
- Chao, S. Y., P. T. Shaw, and S. Y. Wu (1996), Deep water ventilation in the South China Sea, *Deep Sea Res.*, *43*, 445–466.
- Chelton, D. B., M. G. Schlax, M. H. Freilich, and R. F. Milliff (2004), Satellite measurements reveal persistent small-scale features in ocean winds, *Science*, *303*, 978–983.
- Chu, P. C., N. L. Edmons, and C. W. Fan (1999), Dynamical mechanisms for the South China Sea seasonal circulation and thermohaline variabilities, *J. Phys. Oceanogr.*, *29*, 2971–2989.
- Dijkstra, H. A., and M. Ghil (2005), Low-frequency variability of the large-scale ocean circulation: A dynamical systems approach, *Rev. Geophys.*, *43*, RG3002, doi:10.1029/2002RG000122.
- Ducet, N., P. Y. Le Traon, and G. Reverdin (2000), Global high-resolution mapping of ocean circulation from TOPEX/Poseidon and ERS-1 and-2, *J. Geophys. Res.*, *105*, 19,477–19,498.
- Fang, W. D., G. H. Fang, P. Shi, Q. Z. Huang, and Q. Xie (2002), Seasonal structures of upper layer circulation in the southern South China Sea from in situ observations, *J. Geophys. Res.*, *107*(C11), 3202, doi:10.1029/2002JC001343.
- Fu, X. H., B. Wang, T. Li, and J. P. McCreary (2003), Coupling between northward-propagating, intraseasonal oscillations and sea surface temperature in the Indian Ocean, *J. Atmos. Sci.*, *60*, 1733–1753.
- Gan, J., H. Li, E. N. Curchitser, and D. B. Haidvogel (2006), Modeling South China Sea circulation: Response to seasonal forcing regimes, *J. Geophys. Res.*, *111*, C06034, doi:10.1029/2005JC003298.
- Gao, T. Z., and F. X. Zhou (2002), Monsoonal characteristics revealed by intraseasonal variability of Sea Surface Temperature (SST) in the South China Sea (SCS), *Geophys. Res. Lett.*, *29*(8), 1222, doi:10.1029/2001GL014225.
- Ho, C. R., Q. N. Zheng, Y. S. Soong, N. J. Kuo, and J. H. Hu (2000), Seasonal variability of sea surface height in the South China Sea observed with TOPEX/Poseidon altimeter data, *J. Geophys. Res.*, *105*, 13,981–13,990.
- Isoguchi, O., and H. Kawamura (2006), MJO-related summer cooling and phytoplankton blooms in the South China Sea, *Geophys. Res. Lett.*, *33*, L16615, doi:10.1029/2006GL027046.
- Jiang, X., T. Li, and B. Wang (2004), Structures and mechanisms of the northward propagating boreal summer intraseasonal oscillation, *J. Clim.*, *17*, 1022–1039.
- Kuo, N. J., Q. N. Zheng, and C. R. Ho (2000), Satellite observation of upwelling along the western coast of the South China Sea, *Remote Sens. Environ.*, *74*, 463–470.
- Lau, W. K. M., and D. E. Waliser (2005), *Intraseasonal Variability of the Atmosphere-Ocean Climate System*, 474 pp., Springer, Heidelberg, Germany.
- Lin, I.-I., W. T. Liu, C.-C. Wu, J. C. H. Chiang, and C.-H. Sui (2003), Satellite observations of modulation of surface winds by typhoon-induced upper ocean cooling, *Geophys. Res. Lett.*, *30*(3), 1131, doi:10.1029/2002GL015674.
- Liu, W. T., and X. Xie (1999), Space-based observations of the seasonal changes of South Asian monsoons and oceanic response, *Geophys. Res. Lett.*, *26*, 1473–1476.
- Liu, Z. Y., H. J. Yang, and Q. Y. Liu (2001), Regional dynamics of seasonal variability in the South China Sea, *J. Phys. Oceanogr.*, *31*, 272–284.
- Metzger, E. J. (2003), Upper ocean sensitivity to wind forcing in the South China Sea, *Oceanogr. J.*, *59*, 783–798.
- Niiler, P. P., N. A. Maximenko, and J. C. McWilliams (2003), Dynamically balanced absolute sea level of the global ocean derived from near-surface velocity observations, *Geophys. Res. Lett.*, *30*(22), 2164, doi:10.1029/2003GL018628.
- Nonaka, M., and S. P. Xie (2003), Covariations of sea surface temperature and wind over the Kuroshio and its extension: Evidence for ocean-to-atmosphere feedback, *J. Clim.*, *16*, 1404–1413.
- Qu, T. D. (2000), Upper-layer circulation in the South China Sea, *J. Phys. Oceanogr.*, *30*, 1450–1460.
- Qu, T. D. (2001), Role of ocean dynamics in determining the mean seasonal cycle of the South China Sea surface temperature, *J. Geophys. Res.*, *106*, 6943–6955.
- Sengupta, D., B. N. Goswami, and R. Senan (2001), Coherent intraseasonal oscillations of ocean and atmosphere during the Asian summer monsoon, *Geophys. Res. Lett.*, *28*, 4127–4130.
- Shaw, P. T., and S. Y. Chao (1994), Surface Circulation in the South China Sea, *Deep-Sea Res., Part I*, *41*, 1663–1683.
- Shaw, P. T., S. Y. Chao, and L. L. Fu (1999), Sea surface height variations in the South China Sea from satellite altimetry, *Oceanol. Acta*, *22*, 1–17.
- Small, R. J., S. P. Xie, and J. Hafner (2005), Satellite observations of mesoscale ocean features and copropagating atmospheric surface fields in the tropical belt, *J. Geophys. Res.*, *110*, C02021, doi:10.1029/2004JC002598.
- Straub, K. H., and G. N. Kiladis (2003), Interactions between the boreal summer intraseasonal oscillation and higher-frequency tropical wave activity, *Mon. Weather Rev.*, *131*, 945–960.
- Taguchi, B., S.-P. Xie, N. Schneider, M. Nonaka, H. Sasaki, and Y. Sasai (2007), Decadal variability of the Kuroshio Extension: Observations and an eddy-resolving model hindcast, *J. Clim.*, *20*, 2357–2377.
- Tang, D. L., H. Kawamura, H. Doan-Nhu, and W. Takahashi (2004), Remote sensing oceanography of a harmful algal bloom off the coast of southeastern Vietnam, *J. Geophys. Res.*, *109*, C03014, doi:10.1029/2003JC002045.
- Vecchi, G. A., and D. E. Harrison (2002), Monsoon breaks and subseasonal sea surface temperature variability in the Bay of Bengal, *J. Clim.*, *15*, 1485–1493.
- Vecchi, G. A., S. P. Xie, and A. S. Fischer (2004), Ocean-atmosphere covariability in the western Arabian Sea, *J. Clim.*, *17*, 1213–1224.
- Waliser, D. E., R. Murtugudde, and L. E. Lucas (2004), Indo-Pacific Ocean response to atmospheric intraseasonal variability: 2. Boreal summer and the Intraseasonal Oscillation, *J. Geophys. Res.*, *109*, C03030, doi:10.1029/2003JC002002.
- Wang, B. (2006), *The Asian Monsoon*, 787 pp., Springer, New York.
- Wang, D. X., Y. Du, and P. Shi (2002), *Climatological Atlas of Physical Oceanography in the Upper Layer of the South China Sea*, 168 pp., Chin. Meteorol. Press, Beijing, China.
- Wang, D. X., W. Wang, P. Shi, P. Guo, and Z. Gan (2003), Establishment and adjustment of monsoon-driven circulation in the South China Sea, *Sci. China, Ser. D*, *46*, 173–181.
- Wang, G. H. (2004), Mesoscale eddies in the South China Sea, 96 pp., Ph.D. thesis, Ocean Univ. of China, Qingdao, China.
- Wang, G. H., D. Chen, and J. L. Su (2006), Generation and Life Cycle of the Dipole in the South China Sea Summer Circulation, *J. Geophys. Res.*, *111*, C06002, doi:10.1029/2005JC003314.
- Wang, W., and C. Wang (2006), Formation and decay of the spring warm pool in the South China Sea, *Geophys. Res. Lett.*, *33*, L02615, doi:10.1029/2005GL025097.
- Wentz, F. J., C. Gentemann, D. Smith, and D. Chelton (2000), Satellite measurements of sea surface temperature through clouds, *Science*, *288*, 847–850.
- Wyrtki, K. (1961), Physical oceanography of the Southeast Asian waters, *Naga Rep.* *2*, 195 pp., Scripps Inst. of Oceanogr., La Jolla, Calif.
- Xie, P. P., and P. A. Arkin (1997), Global precipitation: A 17-year monthly analysis based on gauge observations, satellite estimates, and numerical model outputs, *Bull. Am. Meteorol. Soc.*, *78*, 2539–2558.
- Xie, S. P. (1999), A dynamic ocean-atmosphere model of the tropical Atlantic decadal variability, *J. Clim.*, *12*, 64–70.

- Xie, S. P. (2004), Satellite observations of cool ocean-atmosphere interaction, *Bull. Am. Meteorol. Soc.*, 85, 195–208.
- Xie, S. P., J. Hafner, Y. Tanimoto, W. T. Liu, H. Tokinaga, and H. M. Xu (2002), Bathymetric effect on the winter sea surface temperature and climate of the Yellow and East China Seas, *Geophys. Res. Lett.*, 29(24), 2228, doi:10.1029/2002GL015884.
- Xie, S. P., Q. Xie, D. X. Wang, and W. T. Liu (2003), Summer upwelling in the South China Sea and its role in regional climate variations, *J. Geophys. Res.*, 108(C8), 3261, doi:10.1029/2003JC001867.
- Xie, S. P., H. M. Xu, N. H. Saji, Y. Q. Wang, and W. T. Liu (2006), Role of narrow mountains in large-scale organization of Asian monsoon convection, *J. Clim.*, 19, 3420–3429.
- Xu, X., Z. Qiu, and H. Chen (1982), The general descriptions of the horizontal circulation in the South China Sea, in *Proceedings of the Marine Hydrographic and Meteorological Society of China*, pp. 137–145, Science Press, Beijing.
-
- C.-H. Chang and S.-P. Xie, International Pacific Research Center and Department of Meteorology, University of Hawaii, HI 96822, USA. (xie@hawaii.edu)
- D. Wang and Q. Xie, Laboratory for Tropical Marine Environmental Dynamics, South China Sea Institute of Oceanology, Chinese Academy of Sciences, Guangzhou 510301, China. (dxwang@scsio.ac.cn; gordonxie@scsio.ac.cn)